The Astrophysical Journal Letters, 997:L28 (7pp), 2026 January 20 https://doi.org/10.3847/2041-8213/ae3136

Observation of Large-scale Kelvin–Helmholtz Instability Wave Driven by a Coronal Mass Ejection

Leon Ofman[1,2,8], Olga Khabarova[3], Ryun-Yong Kwon[4], Yogesh[5], Eyal Heifetz[6], and Katariina Nykyri[7]
[1] Institute for Astrophysics and Computational Sciences, Department of Physics, Catholic University of America, Washington, DC 20064, USA; ofman@cua.edu
[2] Heliophysics Science Division, NASA Goddard Space Flight Center, Greenbelt, MD 20771, USA
[3] Interdisciplinary Centre for Security, Reliability and Trust, University of Luxembourg, Luxembourg, Luxembourg
[4] Korea Astronomy and Space Science Institute(KASI), Daejeon, Republic of Korea
[5] Department of Physics and Astronomy, University of Iowa, Iowa City, IA 54224, USA
[6] Department of Geosciences, Tel Aviv University, Ramat Aviv, Tel Aviv, Israel
[7] Embry-Riddle Aeronautical University, Daytona Beach, FL, USA
Received 2025 November 17; revised 2025 December 18; accepted 2025 December 22; published 2026 January 20

Abstract

The Kelvin–Helmholtz instability (KHI) can occur when there is a relative motion between two adjacent fluids. In the case of magnetized plasma, the shear velocity must exceed the local Alfvén speed for the instability to develop. The KHI produces nonlinear waves that eventually roll up into vortices and contribute to turbulence and dissipation. In the solar atmosphere, KHI has been detected in coronal mass ejections (CMEs), jets, and prominences, mainly in the low corona. Only a few studies have reported the KHI in the upper corona, and its vortex development there has not been previously observed. We report an event with large-scale KHI waves observed from ∼6 to 14 $R_\odot$ on 2024 February 16 using Solar and Heliospheric Observatory/Large Angle and Spectrometric Coronagraph and STEREO-A coronagraphs. A KHI appeared during the passage of a fast CME and evolved into the nonlinear stage showing evidence of vortices. A closely timed subsequent CME in the same region further developed the fully nonlinear KHI waves along its flank. We find that the radial speed of the CMEs exceeds the estimated local Alfvén speed obtained from in-situ Parker Solar Probe magnetic field data at perihelia. We propose that such events are rare because the fast CME created specific conditions favorable for instability growth in its trailing edge, including radial elongation of magnetic-field lines, reduced plasma density, and enhanced velocity and magnetic-field shear along the developing interface. The observed growth rate of the KHI wave is in qualitative agreement with the theoretical predictions.

Unified Astronomy Thesaurus concepts: Active solar corona (1988); Solar coronal mass ejections (310); Solar coronal waves (1995)

Materials only available in the online version of record: animations

1. Introduction

The coronal mass ejections (CMEs) are routinely observed with space-based coronagraphs such as the Large Angle and Spectrometric Coronagraph (LASCO) on board the Solar and Heliospheric Observatory (SOHO; V. Domingo et al. 1995), and Sun Earth Connection Coronal and Heliospheric Investigation COR1 and COR2 coronagraphs on the Solar Terrestrial Relations Observatory (STEREO; M. L. Kaiser et al. 2008) spacecraft. During periods of increased solar activity, CMEs can reach speeds of several hundred to ∼2000 km s^{-1} and form fast shocks with Alfvénic Mach number $M_A > 1$, i.e., with eruption velocities exceeding the local Alfvén speed, V_A. These energetic eruptions, observed as they form in the solar corona, propagate throughout the heliosphere reaching the Earth's orbit and beyond. CMEs' fast propagation results in a velocity shear between the nearly stationary background coronal structures, such as adjacent streamers, and this can lead to the development of shear-driven magnetized fluid instability as well as generation of streamer waves. Several studies have analyzed coronal streamer waves produced by CMEs (Y. Chen et al. 2010, 2011; R.-Y. Kwon et al. 2013a, 2013b; A. K. Srivastava et al. 2016; B. Decraemer et al. 2020), showing that the characteristics of these waves can be used to extract valuable seismological information, such as the magnetic field in both the streamers and the CME ejecta–sheath interface (K. Nykyri & C. Foullon 2013).

The Kelvin–Helmholtz instability (KHI) can grow due to shear flows in magnetized fluids when the velocity shear (or velocity jump) magnitude exceeds the local Alfvén speed in the parallel direction (S. Chandrasekhar 1961). Magnetized KHI instability was previously detected in the Earth's magnetospheric boundary where it plays an important role in energy transport (see the review, K. Nykyri et al. 2021). In the context of solar phenomena, KHI often arises due to differences in the plasma velocity configuration between adjacent regions or within magnetoplasma structures that move at different speeds relative to the surrounding plasmas. Several studies have documented the development of the KHI in solar prominences (T. E. Berger et al. 2010; T. Berger et al. 2017; A. Hillier & V. Polito 2018; H. Yang et al. 2018), in coronal jets (X. Li et al. 2018; M. Bogdanova et al. 2018; I. Zhelyazkov & R. Chandra 2018; I. Zhelyazkov et al. 2018; S. K. Mishra et al. 2025), in CMEs (e.g., C. Foullon et al. 2011; L. Ofman & B. J. Thompson 2011; U. V. Möstl et al. 2013; K. Nykyri 2024), streamers (e.g., L. Feng et al. 2013), and at the edges of coronal holes (D. Telloni et al. 2022) and switchback

[8] Visiting, Department of Geosciences, Tel Aviv University, Tel Aviv, Israel.

boundaries (F. S. Mozer et al. 2020; K.-E. Choi et al. 2025); they have also been detected in situ by the Solar Orbiter spacecraft in the solar wind (R. Kieokaew et al. 2021). Recently, KHI signatures of small-scale vortices were directly imaged close to the Sun in the range 7.5–9.5 R_s (where R_s is the solar radius) with the Parker Solar Probe (PSP; N. J. Fox et al. 2016) Wide Field Imager (A. Vourlidas et al. 2016) in a slow CME (~ 200 km s^{-1}) that propagated along a preexisting streamer (E. Paouris et al. 2024).

Understanding the development of KHI in the solar corona is important for explaining various solar phenomena, as it directly impacts energy transfer processes and the stability of the solar atmosphere. In particular, the KHI may lead to the formation of nonlinear waves that eventually break and create turbulence, which is, in turn, linked to corona heating, the most debated topic in the solar community (see the review, T. Van Doorsselaere et al. 2020).

The present study is motivated by observations of a large-amplitude wave in a dense coronal structure at distances ~6–14 R_s associated with the propagation of two fast CMEs subsequently ejected from the same active region detected on 2024 February 16 with COR1 and COR2 coronagraphs on board STEREO-A and with the LASCO C2 and C3 coronagraphs on board SOHO. This is the first observational analysis of the growth and saturation of large-amplitude nonlinear wave structure (vortex) that is a typical signature of KHI and subsequent dissipation of this structure in this region. The results impact the understanding of evolution of magnetized flows and CMEs in the lower corona and the potentially important role of KHI in the energy transfer in the solar corona in eruptive events. The Letter is organized as follows. In Section 2, we analyze the CME evolution, and in Section 2.1, we present the analysis of the observed KHI wave. In Section 2.2, we present the PSP results of the coronal properties. Section 3 is devoted to theoretical analysis, and the discussion and conclusions are in Section 4.

2. Observational Data Analysis: CME Evolution

The fast partial-halo CME on 2024 February 16 with onset time 7:12:05 was observed by STEREO-A COR1 and COR2 coronagraphs, as well as by SOHO/LASCO C2 and C3 coronagraphs. The parameters of the CME and the animations are available on the SOHO LASCO CME catalog at https://cdaw.gsfc.nasa.gov/CME_list. In Figure 1(a), the CME and the associated wave marked with the yellow arrow are shown from STEREO COR1 data with the inner corona imaged with EUVI 171 Å emission. The developed KHI large-amplitude wave structure extends nearly radially, marked by the yellow arrow. Figure 1(b) show the LASCO C2 and C3 images with the inner corona from the Solar Dynamics Observatory (SDO) Atmospheric Imaging Assembly (AIA) 193 Å emission. The heliocentric distances in Figures 1(a) and (b) are matched to facilitate comparison. A large-amplitude KHI wave structure indicated by the yellow arrows in the upper panels extends nearly radially, likely associated with partially erupted prominence material. The nearly radial KHI large-amplitude wave structure is also evident in the LASCO C3 image. The heliocentric separation between the two spacecraft was ~8°, shown schematically in Figure 1(c). The animations for this figure were produced using JHelioviewer software.[9]

[9] See https://www.jhelioviewer.org.

The well-developed KHI event on 2024 February 16 is associated with two consecutive CMEs originating from a broad active region located near S19W85, close to the southwestern solar limb. The primary CME ($v \approx 620$ km^{-1}) was driven by an intense X2.5-class flare that occurred at 06:42 UT on 2024 February 16. According to the NASA GOES flare catalog,[10] based on GOES X-ray flux measurements, the active region exhibited elevated flare activity beginning 1 day earlier, producing several C- and M-class flares; the X2.5-class flare associated with the event discussed here represented the peak of its eruptive evolution. A video of the flare sequence together with the corresponding GOES X-ray flux at Earth orbit is available in the SDO archive.[11]

The manually compiled SOHO/LASCO CME catalog maintained by the CDAW Data Center[12] lists the first appearance of the main CME in coronagraph images at 2024 February 16 07:12:05 UT. A second—weaker and slower—CME ($v \sim 450$ km s^{-1}) erupted approximately 5 hr later.[13] Owing to its low brightness relative to the primary CME, this secondary eruption was not identified as a separate event in widely used CME catalogs and is therefore treated here as part of the main eruption sequence. The KHI initiated forming waves and vortices during the propagation of the main CME, while the subsequent CME extended the duration of the fast outflow, contributing to further KHI wave growth.

In Figure 1(c), the height–time plot for this CME is shown. The least-square fit velocity is 620 km s^{-1}, while a second-order polynomial produced a slightly decelerating velocity profile resulting in about 670 km s^{-1} at 10 R_s, with both fits producing similar high correlation coefficient R^2 values near unity. The approximate onset time of the second CME and the detection time of the developed KHI wave with vortices (see Figure 2 below) are indicated with the red arrows. We note that the CME front has traveled away from the lower heights of KHI wave growth, with the CME front detected at >20 R_s at the indicated time of the developed KHI wave. The KHI develops over the entire range of distances shown in Figures 1(a)–(b), and the red arrows merely show the timing for the reader's convenience.

2.1. Observed KHI Wave Properties

The observed KHI wave properties were obtained from the spacetime analysis of the wave feature shown in Figure 1. In Figure 2(a), the wave feature is shown in a zoomed-in field of view, focusing on the wave structure with two virtual slits marked on the image with the vertical lines. The location of Slit 1 is in an adjacent erupting region and is used to provide the spacetime plot in Figure 2(b). The location of Slit 2 is chosen to cut through the wave features, which allows determination of the time-dependent wavelength (see the colored dots) and the velocities of the wave structure from the spacetime plots shown in Figure 2(c).

In Figure 3, we show five snapshots from the STEREO COR1 animation at hourly intervals, starting at 13:07 UT on

[10] https://umbra.nascom.nasa.gov/goes/eventlists/goes_event_listings/goes_xray_event_list_2024.txt

[11] https://sdowww.lmsal.com/sdomedia/ssw/media/ssw/ssw_client/data/ssw_service_240216_202757_30626/www/EDS_FlareDetective-TriggerModule_20240214T131759-20240217T041235_AIA_211_XCEN883.2YCEN-268.8_ssw_cutout_20240214_131759_AIA_211__20240214_131757_m.mp4

[12] https://cdaw.gsfc.nasa.gov/CME_list/UNIVERSAL_ver2/2024_02/univ2024_02.html

[13] See Figure 1(b) animation and https://www.sidc.be/cactus/.

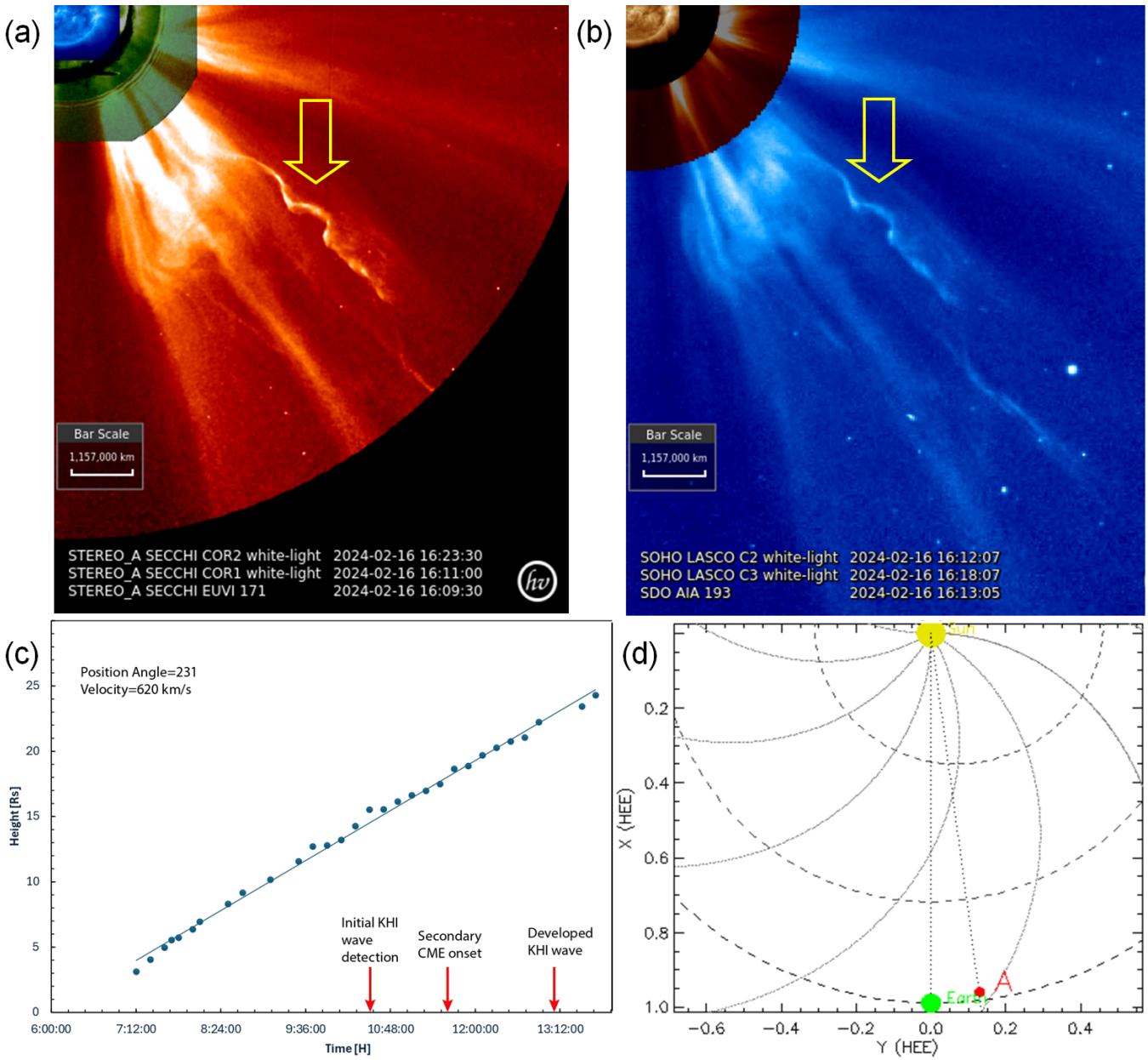

Figure 1. The CME and the associated wave marked with the yellow arrow observed on 2024 February 16. The timing of the various instruments are indicated on the panels. (a) STEREO COR2 (the inner regions are obtained from EUVI and COR1 images). (b) The SOHO/LASCO C3 observations (the inner regions are obtained from LASCO C2, C3 and SDO AIA 193 Å images). The animations of this event produced by JHelioviewer (see https://www.jhelioviewer.org) are available. (c) Height–time plot of the main CME observed on 2024 February 16. The CME speed in the plane of the sky obtained from linear least-square fit is 620 km s^{-1}, with $R^2 = 0.9959$. The red arrows indicate the approximate onset times of the second CME, initial wave formation, and the observed developed KHI wave. (d) STEREO-A view of the Sun (red dot) on 2024 February 16 with ∼8° separation angle with respect to LASCO. Animations of the STEREO EUVI/COR1/COR2 (panel (a), full-field) and the SOHO/LASCO C2/C3 and SDO/AIA 193 Å images (panel (b)) are available. The animations appear sequentially—first, the full-field STEREO animations proceed from 14:09 to 21:17 UT; this animation loops five times for clarity and shows the developing wave with KHI features in the COR2 coronagraph field of view; second, the SOHO/LASCO C2/C3 animated images run from 04:22 UT on February 16 to 07:54 UT on February 17, showing the KHI wave feature in C2/C3 coronagraphs field of view.

(An animation of this figure is available in the online article.)

2024 February 16, of the wave structure showing the development stages of KHI waves and vortices with their locations marked with yellow arrows. The signatures of KHI waves and the associated vortices are discernible. The wavelength of the KHI wave increases from ∼1 R_s at 13.07 UT to ∼1.9 R_s at 17:07 UT (see Figure 4(a)).

In Figure 4(a), the temporal evolution of the wavelength (in R_s units) is shown (also, see Figure 2(a) and the corresponding animation). It is evident that the wavelength increases nearly linearly with time from ∼0.6 R_s to ∼2.5 R_s, over the time interval of ~7.25 hrs where the peak wave amplitude occurs at ∼16.5 hr UT for a wavelength of 1.7 R_s. From the temporal evolution (see the animation), it appears that there are two stages of evolution of the KHI wave: initial growth of the KHI wave amplitude during the CME eruption, followed by the damping the KHI wave amplitude at later times after the waning of the CME eruption and of the radial expansions of the wave structure.

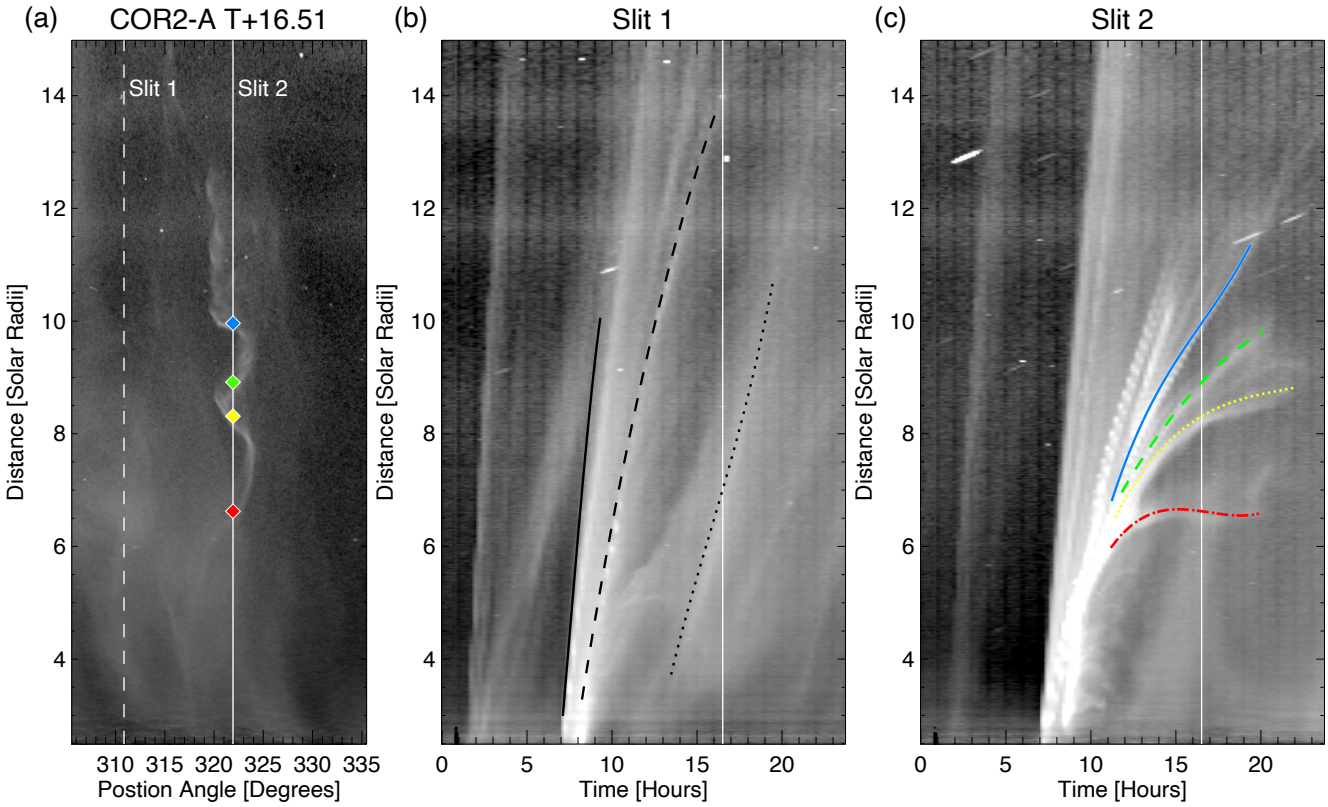

Figure 2. (a) Portion of the STEREO COR2-A field of view at 16:38 UT on 2024 February 16, highlighting the KHI wave event. The vertical dashed and solid lines refer to the two virtual slit positions used to construct the distance–time plots in panels (b) and (c). The position of Slit 1 (dashed line) is fixed, while Slit 2 (solid line) crosses the KHI wave features. Colored dots along Slit 2 mark the locations used to track the wave structure. (b) Distance–time plot of the propagating features along Slit 1, where features #1 (solid), #2 (dashed), and #3 (dotted) are identified. (c) Distance–time plot of the KHI wave features along Slit 2, showing the evolution of features #1 (blue), #2 (green), #3 (yellow), and #4 (red), which correspond to the colored dots with the same color. Colored curves indicate the fitted propagation tracks used to derive their velocities. The vertical solid line in panels (b) and (c) correspond to the time of panel (a). An animation of this figure is available. The animation proceeds over 24 hr period starting 16 hr before and ending 8 hr after the KHI wave event, showing the erupting features associated with the CME and the growth and dissipation of the KHI wave to demonstrate the increase in wavelength.

(An animation of this figure is available in the online article.)

The radial outflow velocity V_r of the features in the stationary Slit 1 is determined by evaluating the numerical derivatives of the spacetime plot fits along the lines (indicated in b/w line-styles) shown in Figures 4(b) and (c), respectively. The radial velocity V_r for Slit 1 is shown in Figure 2(a). It is evident that after ∼7.5 hr, the V_r reaches the peak value close to 1000 km s^{-1}, followed by decrease to ∼600–700 km s^{-1}. However, the second and third features have much lower velocities decreasing from ∼400 km s^{-1} to the range of 150–200 km s^{-1}, consistent with the local solar wind speed. The third feature corresponds to the flank of the second weaker CME.

The flow velocities of the features in Slit 2 are shown in Figure 2(c). Since this slit is along the KHI wave feature, it is evident that the velocities are generally slower than along Slit 1. The first feature associated with the KHI wave is detected in the slit at about 10 hr after the onset of the main CME event, reaching 300 km s^{-1}, and slows down to ∼160 km s^{-1} at $t \approx 16$ hr. Feature #1 detected in the slit starts with $V \approx 170$ km s^{-1} and decelerates to ∼100 km s^{-1}, while the remaining features, #2–#3, are all slow, with velocities below 100 km s^{-1}. Feature #4 becomes nearly stationary at $t = 16$ hr. Thus, due to the variation of the outflow speed between the features, it is evident that there is significant initial acceleration and deceleration of the erupting material as well as significant shear velocity between the outflowing materials as demonstrated by the analysis of the two slits. Base on the observed CME feature velocities in Slit 1 in the range of ∼400–1000 km s^{-1} and the KHI wave feature velocities in Slit 2 in the range ∼0–170 km s^{-1}, the velocity shear can be estimated in the range ∼230–830^{-1} and is likely super-Alfvénic, favorable for KHI growth (see the theoretical analysis in Section 3 below).

2.2. Alfvén and Solar Wind Speeds from PSP Data

Before the PSP era, the Alfvén speed and the solar wind speed in the region of interest of CME eruption close to the Sun were determined indirectly and empirically using remote sensing (e.g., N. R. Sheeley et al. 1997; M. R. Collier et al. 2001; N. Gopalswamy & S. Yashiro 2011). Since the launch of PSP, we now have direct in-situ measurements of the main solar wind parameters at perihelia as close as 9.86 R_s. Since there were no in-situ PSP observations during the exact time of the present event, we use the ensemble of PSP data for statistical determination of solar wind parameters in this region. In Figure 5, the statistical distribution versus heliocentric distance of the Alfvén speed, V_A, and the radial solar wind speed, V_r, are shown. The values are deduced from PSP SPAN-I (which provided the proton velocities) and the FIELDS instrument, which provided the magnetic field

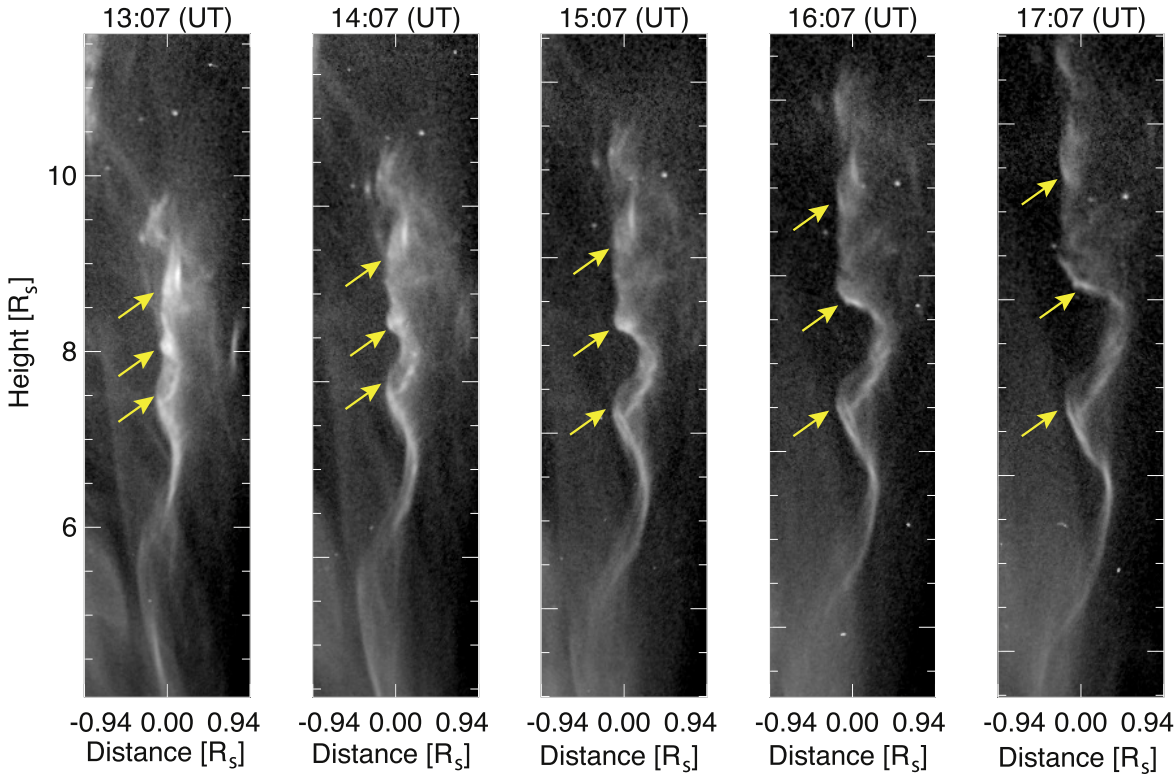

Figure 3. Five snapshots from the STEREO COR1 animation of the KHI feature shown in Figure 2(a) at hourly intervals, starting at 13:07 UT on 2024 February 16, showing the development of the KHI wave structure and the development stages of KHI waves and vortices, with their locations marked with yellow arrows.

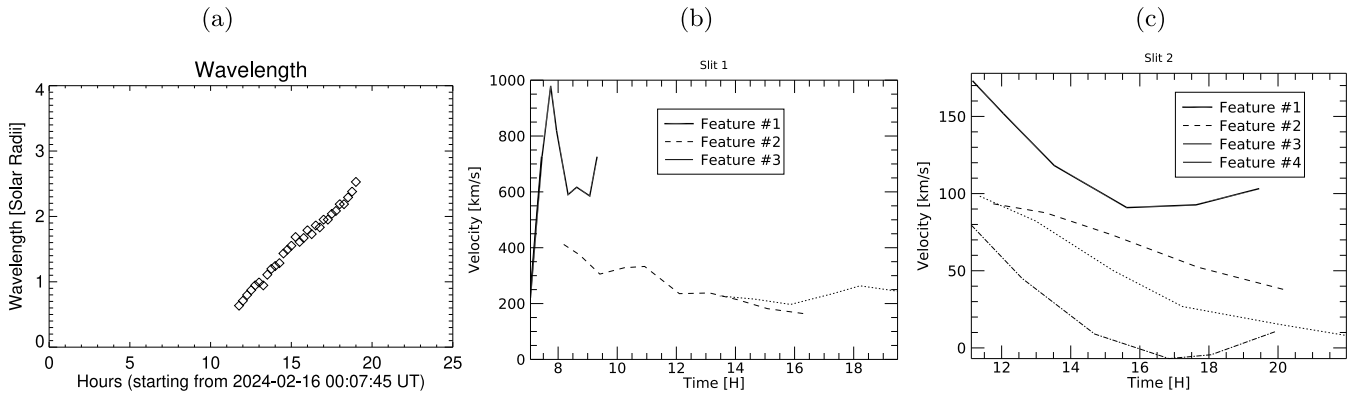

Figure 4. (a) The temporal evolution of the wavelength of the KHI wave observed on 2024 February 16 by STEREO COR2-A, determined as shown at Slit 2 in Figure 2(b). The temporal evolution of the velocities: (b) the radial velocities of the features along Slit 1 (#1 solid, #2 dashed, #3 dotted) and (c) the evolution of velocities along Slit 2 (#1 solid, #2 dashed, #3 dotted, #4 dotted–dashed). The line styles are the same as in Figure 2.

magnitude in the distance range 10–30 R_s obtained during encounters 4–23. The local Alfvén speed values are calculated by using the expression $V_A = B/(4\pi\rho)^{1/2}$ with the in-situ values of the magnetic field magnitude, B, from PSP/FIELDS, and electron density ρ deduced from quasi-thermal noise data. The power-law fit to the Alfvén speed V_A is shown in Figure 5(a) with power $b = -1.05$. The radial solar wind speed V_r is fit with Equation (2) from N. R. Sheeley et al. (1997), i.e., $V_r^2 = 2a(r - r_1)$; the fit parameters are $a \approx 6 \times 10^2$ and $r_1 \approx -40$ shown in Figure 5(b). The dashed vertical line marks the mean Alfvén critical surface of the solar wind at 16.5 R_s, where $M_A = 1$. The color bar scale shows the number of counts for each quantity.

Since there were only few encounters at distances of $\sim$10 R_s, we quote the statistical values of Alfvén speed at 11.25 R_s using PSP data for encounters 4–23 (Yogesh et al. 2026): the median value for the Alfvén speed is 331 km s^{-1}, while p10 (10th percentile) value is 235 km s^{-1}, and the p90 value is 560 km s^{-1}. For V_r at 11.25 R_s the p10 value was 126 km s^{-1}, the median value was 191 km s^{-1}, and p90 value was 283 km s^{-1}. The general trends of PSP data in this distance range indicate that the median V_A value is near the upper limit, while the median V_r value is near the lower limit. These PSP-derived values of the Alfvén speed are consistent with previous estimates and observations at $\sim$10 R_s, such as M. R. Collier et al. (2001), who estimate $V_A = 230$ km s^{-1} at 10 R_s.

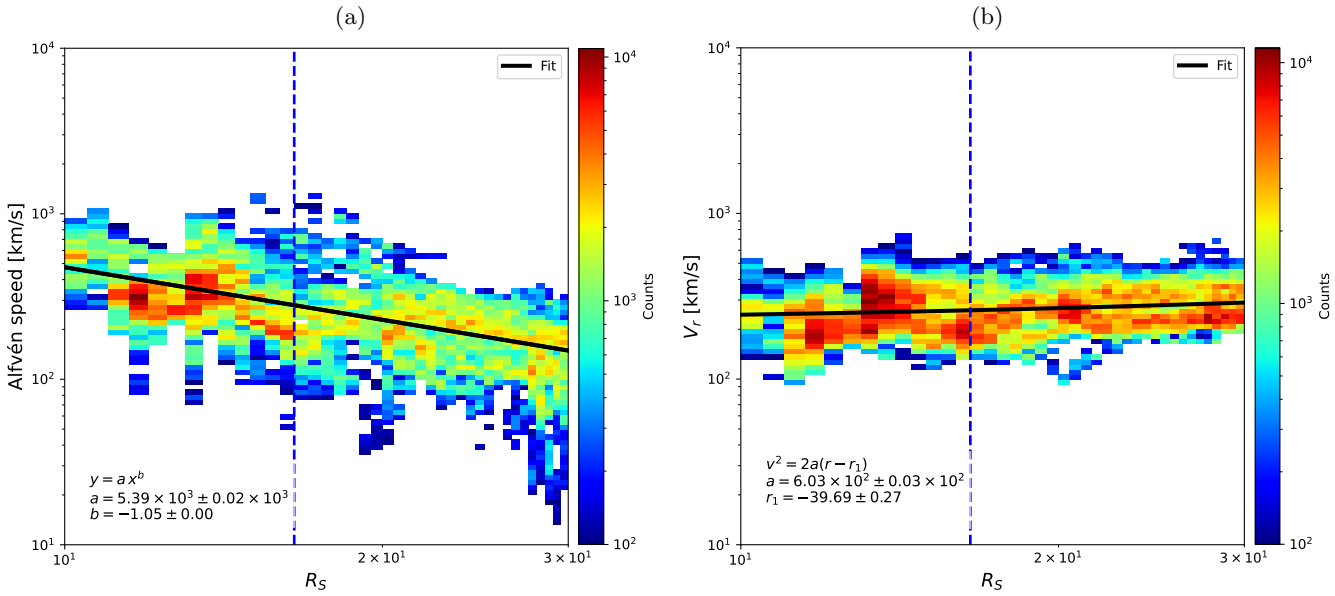

Figure 5. The statistical distribution versus heliocentric distance obtained from PSP in the range 10–30 R_s obtained from encounters 4–23. (a) The Alfvén speed with power-law fit; (b) radial solar wind speed with the N. R. Sheeley et al. (1997) fit. The dashed vertical line marks the mean Alfvén critical surface at 16.5 R_s, where $M_A = 1$. The color bar shows the number of counts. The black lines show the fits, and the fit parameters are indicated on the panels.

3. Theoretical KHI Analysis

The linear growth rate of KHI in the presence of magnetic field for a discontinuous shear layer derived and used previously (e.g., S. Chandrasekhar 1961; A. Frank et al. 1996; L. Ofman & B. J. Thompson 2011) can be written as

$$\gamma = \frac{1}{2}\,|\,\boldsymbol{k}\,\cdot\,\boldsymbol{\Delta V}\,|\,[1 - (2V_A\hat{\boldsymbol{k}}\cdot\hat{\boldsymbol{B}})^2/(\hat{\boldsymbol{k}}\cdot\boldsymbol{\Delta V})^2]^{1/2}, \quad (1)$$

where $\boldsymbol{\Delta V}$ is the velocity jump across the interface, $\boldsymbol{B}$ is the magnetic field, $\boldsymbol{k}$ is the wavevector, the $\hat{}$ indicates a unit vector, and V_A is the Alfvén speed. The above expression provides an upper limit for a finite width velocity interface. It is evident that the parallel flow speed jump must exceed the local Alfvén speed $V_A = B/(4\pi\rho)^{1/2}$, where ρ is the density, so that the KHI can grow.

From observations, we estimate the magnitude $\Delta V \approx 435$ km s^{-1}; the wavevector magnitude is given by $k = 2\pi/\lambda$, where the estimated wavelength $\lambda \sim 0.6\ R_s = 420{,}000$ km. Assuming $\boldsymbol{k}\cdot\boldsymbol{B} \approx 0$, we get the growth rate $\gamma \approx 0.0033$ s^{-1} equal to e-folding growth time of ~5 minutes, and the KHI nonlinear saturation time is several e-folding growth times. The estimated growth rate is in qualitative agreement with the observed growth and evolution of the KHI wave due to the super-Alfvénic CME eruption on 2024 February 16. For the specific conditions $k\|\boldsymbol{\Delta V}\|B$, the growth rate can be estimated from the simplified expression

$$\gamma = \frac{1}{2}|k\Delta V|\,[1 - (2V_A)^2/(\Delta V)^2]^{1/2}. \quad (2)$$

It is also useful to calculate the wavenumber normalized growth rate and the portion of the π angle (Ω_π, hereafter) radially away from the Sun that is KHI unstable and assuming that $\hat{\boldsymbol{k}}$, $\hat{\boldsymbol{B}}$, and $\Delta\boldsymbol{V}$ are in the same plane and $\Delta\boldsymbol{V}$ is along the x-axis. The angle between $\hat{\boldsymbol{k}}$ above (below) the x-axis and $\Delta\boldsymbol{V}$ is θ ($-\theta$), and the angle between $\hat{\boldsymbol{k}}$ and $\boldsymbol{B}$ is α in the range $[0,\pi/2]$ rad, and $2\theta+\alpha$ is in the range $[0,-\pi/2]$ rad. To evaluate this, we express Equation (1) in the following form:

$$\left(\frac{\gamma}{k}\right)^2 = \frac{1}{4}\,|\boldsymbol{\Delta V}\cos(\theta)|^2 \times [1 - (2V_A\cos(\alpha))^2/(\boldsymbol{\Delta V}\cos(\theta))^2]. \quad (3)$$

Since the values of the magnetic field, the Alfvén speed, k, and angle with B are not directly available from the present observations, we next solve this equation with a Monte Carlo method by creating a large number (N) of values of θ and α angles spanning the range [0, $\pi/2$] rad (above the x-axis) and then repeating for the range [0, $-\pi/2$] rad, where $\hat{\boldsymbol{k}}$ is below x-axis (but $\hat{\boldsymbol{B}}$ is above the x-axis) and collecting all vectors for which $(\gamma/k)^2 > 0$. The number N needs to be large, such that results converge (a similar method has been used in, e.g., B. L. Burkholder et al. 2020, K. Nykyri et al. 2021, and K. Nykyri 2024, where the whole solid angle was searched due to additional degrees of freedom in single point in-situ data). The V_A statistical values from PSP data (p10, median, and p90) and $\Delta V = 435$ km s^{-1} yield the unstable fractions of the solid angle $\Omega_\pi =$ 45%, 31%, and 18%, respectively, for $N = 10^6$, and the results converge when running several times and with increased N. The maximum growth rate naturally corresponds to the situation when $\hat{\boldsymbol{k}}$ and $\hat{\boldsymbol{B}}$ are orthogonal, and the velocity shear is parallel to $\hat{\boldsymbol{k}}$. This yields $\gamma/k = 217$ km s^{-1}, the same result as determined in the second paragraph above. We note that the above idealized theoretical analysis in simplified geometry does not take into account the possible helical structure of the CME and the potential effects of this structure on the growth rate of KHI.

4. Discussion and Conclusion

Using STEREO COR2 and SOHO/LASCO C2/C3 coronagraph imaging observations, we find evidence for KHI in large-amplitude wave growth and dissipation in a narrow elongated coronal feature likely associated with partially erupted prominence material at distances of ~6–14 R_s associated with the CME on 2024 February 16, commencing at 7:12 UT. The

observed KHI wave growth event is rarely detected, with KHI wave signatures detected in a handful events at this range of radial distances in streamers associated with CME events (e.g., L. Feng et al. 2013; E. Paouris et al. 2024). This is the first analysis of a large-scale large-amplitude KHI wave event associated with super-Alfvénic CME through all stages of growth and dissipation. Our analysis provides the detailed wave properties, as well as velocities of the erupting CME and elongated feature close to the Sun. It is apparent from coronagraph observations that the main CME is followed by a secondary, weaker CME several hours later that likely facilitated further growth of KHI waves in the adjacent elongated feature due to the combined prolonged eruption stage.

Since the growth of KHI can be suppressed by a parallel magnetic field, the velocity shear must exceed the local (at ∼6–14 R_s) parallel Alfvén speed to allow the growth of the KHI (S. Chandrasekhar 1961). In order to evaluate the ambient stability conditions associated with the CME, we estimate the local Alfvén speed and the solar wind speed at the observed KHI wave distances using PSP statistical perihelia data from encounters 4–23. We find that PSP perihelia data of V_A and V_r are in qualitative agreement with previous empirical and remote sensing estimates of these quantities. Since the exact parameters of the solar corona, such as magnetic field strength and orientation, are not well known, we explore theoretically the parameter space that allows KHI growth using the Monte Carlo (MC) method. As expected, the fastest growth of KHI takes place for orthogonal wavenumber with respect to the magnetic field. We find from MC modeling that a significant fraction of possible orientations between $\boldsymbol{k}$ and $\boldsymbol{B}$ can result in KHI onset. Our analysis shows that the KHI can grow at a distance beyond 6 R_s where the CME propagation speed is super-Alfvénic, leading to sufficiently large velocity shear with the ambient streamer features, enabling the growth of KHI. The subsequent damping of the KHI wave is consistent with the waning stage of the CME eruption and associated decrease in local velocity shear down to sub-Alfvénic values.

The present CME event is favorable for observing the instability growth in its trailing edge, likely due to the radial elongation of magnetic field lines, reduced plasma density following the passage of the CME, and enhanced velocity and magnetic field shear along the developing interface with the adjacent quasi-stationary, bright, elongated structure. As was discussed in several previous studies and demonstrated here, the KHI can play an important role in the energy transfer between the large-scale CME eruptions and the smaller-scale coronal structures, which can eventually result in coronal and solar wind heating as well in the diagnostic of magnetic field and flows in the lower corona. The present results improve the understanding of the nonlinear large-scale evolution of KHI by using the combination of remote sensing with new in-situ data, together with theoretical analysis, to study the observed large-scale KHI wave in a previously unexplored region close to the Sun where KHI can play an important role in the energetics of the solar corona.

Acknowledgments

The authors L.O. and Y. acknowledge support by NASA grant 80NSSC24K0724 and NSF SHINE grant AGS-2300961, as well as from NASA GSFC through Cooperative Agreement 80NSSC21M0180 to Catholic University of America, Partnership for Heliophysics and Space Environment Research (PHaSER). L.O. and K.N. acknowledge support by NASA Internal Scientist Funding Model (ISFM) at GSFC. O.K. acknowledges support by Center of Absorption in Science, Ministry of Immigration and Absorption of Israel for her work at Tel Aviv University. Y. acknowledges support by NASA Heliophysics Guest Investigator grant 80NSSC23K0447 and the College of Liberal Arts and Sciences at the University of Iowa. K.N. also acknowledges the support from NASA Living with a Star grant 80NSSC23K0899. R.-Y.K. acknowledges support by Korea government (KASA, Korea AeroSpace Administration, grant number RS-2023-00235534, Near-Earth ≳10 MeV Solar Proton Event Prediction by probing into Solar Wind Condition with Automatic CME detection).

Facilities: STEREO, SOHO, SDO, Parker.

ORCID iDs

Leon Ofman https://orcid.org/0000-0003-0602-6693
Olga Khabarova https://orcid.org/0000-0002-3230-2033
Ryun-Yong Kwon https://orcid.org/0000-0002-2106-9168
Yogesh https://orcid.org/0000-0001-6018-9018
Eyal Heifetz https://orcid.org/0000-0002-3584-3978
Katariina Nykyri https://orcid.org/0000-0002-6905-9487

References

Berger, T., Hillier, A., & Liu, W. 2017, ApJ, 850, 60
Berger, T. E., Slater, G., Hurlburt, N., et al. 2010, ApJ, 716, 1288
Bogdanova, M., Zhelyazkov, I., Joshi, R., & Chandra, R. 2018, NewA, 63, 75
Burkholder, B. L., Nykyri, K., Ma, X., et al. 2020, GeoRL, 47, e2020GL087268
Chandrasekhar, S. 1961, Hydrodynamic and Hydromagnetic Stability (Clarendon)
Chen, Y., Feng, S. W., Li, B., et al. 2011, ApJ, 728, 147
Chen, Y., Song, H. Q., Li, B., et al. 2010, ApJ, 714, 644
Choi, K.-E., Agapitov, O. V., Bizien, N., Dudok de Wit, T., & Colomban, L. 2025, ApJ, 992, 208
Collier, M. R., Szabo, A., Farrell, W. M., et al. 2001, JGR, 106, 15985
Decraemer, B., Zhukov, A. N., & Van Doorsselaere, T. 2020, ApJ, 893, 78
Domingo, V., Fleck, B., & Poland, A. I. 1995, SoPh, 162, 1
Feng, L., Inhester, B., & Gan, W. Q. 2013, ApJ, 774, 141
Foullon, C., Verwichte, E., Nakariakov, V. M., Nykyri, K., & Farrugia, C. J. 2011, ApJL, 729, L8
Fox, N. J., Velli, M. C., Bale, S. D., et al. 2016, SSRv, 204, 7
Frank, A., Jones, T. W., Ryu, D., & Gaalaas, J. B. 1996, ApJ, 460, 777
Gopalswamy, N., & Yashiro, S. 2011, ApJL, 736, L17
Hillier, A., & Polito, V. 2018, ApJL, 864, L10
Kaiser, M. L., Kucera, T. A., Davila, J. M., et al. 2008, SSRv, 136, 5
Kieokaew, R., Lavraud, B., Yang, Y., et al. 2021, A&A, 656, A12
Kwon, R.-Y., Kramar, M., Wang, T., et al. 2013a, ApJ, 776, 55
Kwon, R.-Y., Ofman, L., Olmedo, O., et al. 2013b, ApJ, 766, 55
Li, X., Zhang, J., Yang, S., Hou, Y., & Erdélyi, R. 2018, NatSR, 8, 8136
Mishra, S. K., Srivastava, A. K., Rajaguru, S. P., & Jelínek, P. 2025, ApJ, 982, 147
Möstl, U. V., Temmer, M., & Veronig, A. M. 2013, ApJL, 766, L12
Mozer, F. S., Agapitov, O. V., Bale, S. D., et al. 2020, ApJS, 246, 68
Nykyri, K. 2024, GeoRL, 51, e2024GL110477
Nykyri, K., & Foullon, C. 2013, GeoRL, 40, 4154
Nykyri, K., Ma, X., & Johnson, J. 2021, GMS, 2, 109
Nykyri, K., Ma, X., Burkholder, B., et al. 2021, JGRA, 126, e2019JA027698
Ofman, L., & Thompson, B. J. 2011, ApJL, 734, L11
Paouris, E., Stenborg, G., Linton, M. G., et al. 2024, ApJ, 964, 139
Sheeley, N. R., Jr., Wang, Y., Hawley, S. H., et al. 1997, ApJ, 484, 472
Srivastava, A. K., Singh, T., Ofman, L., & Dwivedi, B. N. 2016, MNRAS, 463, 1409
Telloni, D., Adhikari, L., Zank, G. P., et al. 2022, ApJ, 929, 98
Van Doorsselaere, T., Srivastava, A. K., Antolin, P., et al. 2020, SSRv, 216, 140
Vourlidas, A., Howard, R. A., Plunkett, S. P., et al. 2016, SSRv, 204, 83
Yang, H., Xu, Z., Lim, E.-K., et al. 2018, ApJ, 857, 115
Yogesh, Ofman, L., Klein, K. G., et al. 2026, ApJ, submitted
Zhelyazkov, I., & Chandra, R. 2018, MNRAS, 478, 5505
Zhelyazkov, I., Zaqarashvili, T. V., Ofman, L., & Chandra, R. 2018, AdSpR, 61, 628